

Article

# Mössbauer Spectroscopy of Triphylite ( $\text{LiFePO}_4$ ) at Low Temperatures

Tomáš Kmječ<sup>1</sup>, Jaroslav Kohout<sup>1</sup>, Milan Dopita<sup>2</sup>, Miroslav Veverka<sup>1</sup> and Jan Kuriplach<sup>1,\*</sup>

<sup>1</sup> Department of Low Temperature Physics, Faculty of Mathematics and Physics, Charles University, V Holešovičkách 2, CZ-180 00 Prague, Czech Republic; tomas.kmjec@mff.cuni.cz (T.K.); kohout@mbox.troja.mff.cuni.cz (J.K.); veverka@nbox.troja.mff.cuni.cz (M.V.)

<sup>2</sup> Department of Condensed Matter Physics, Faculty of Mathematics and Physics, Charles University, Ke Karlovu 5, CZ-121 16 Prague, Czech Republic; dopita@gmail.com

\* Correspondence: jan.kuriplach@mff.cuni.cz

Received: 1 September 2019; Accepted: 16 October 2019; Published: 18 October 2019



**Abstract:** Low temperature magnetic ordering in the  $\text{LiFePO}_4$  compound is investigated experimentally using Mössbauer spectroscopy and theoretically via first principles calculations. The evaluation of experiment carried out on a powder sample is compatible with an antiferromagnetic order of Fe ion magnetic moments. When an external magnetic field is applied, Fe magnetic moments start to deviate slightly from the [010] easy magnetization direction. These findings are confirmed by means of first principles calculations, which also suggest the magnitude of single ion magnetic anisotropy and orbital and spin-dipolar contributions to the magnetic hyperfine field, which is eventually in a good agreement with the experiment. Diffraction and magnetic measurements complement the study.

**Keywords:**  $\text{LiFePO}_4$ ; Mössbauer spectroscopy; antiferromagnetic order; density functional theory

## 1. Introduction

Triphylite or lithium iron phosphate ( $\text{LiFePO}_4$ , LFP) compound is frequently used as a cathode material for Li-ion batteries [1,2]. It offers some advantages, but also shows a few disadvantages when compared to the most frequently used lithium cobalt oxide ( $\text{LiCoO}_2$ ) based batteries. Triphylite exhibits a relatively low-symmetry orthorhombic structure [1,3], which is the origin of many interesting and sometimes puzzling properties. For example, LFP is changing its bond character from ionic to more covalent upon delithiation, thus affecting various battery characteristics [4–6]. Another example can be Li diffusion capability, which seems to be hampered by grain boundaries [6,7].

Even if magnetic properties of  $\text{LiFePO}_4$  do not affect directly the operation of batteries since the working temperature is well above the ordering temperature, it is worth studying such magnetic phenomena because of their involvement in structural and electronic properties [8]. Magnetic properties of LFP were studied by Santoro and Newnham [9] and Rouse et al. [10] using neutron scattering on polycrystalline/powdered samples. Both works found an antiferromagnetic structure with the Néel temperature ( $T_N$ ) close to 50 K. Later more precise experiments [11–13] performed on single crystals have unveiled a more complicated magnetic structure. Magnetic moments (MMs) are not exactly oriented along the crystallographic axis  $b$  ( $Pnma$  space group considered), but there are both collinear rotations from this axis and canting of MMs. The overall deviation from the axis  $b$  is rather small and amounts to only  $1.3^\circ$  [13]. In this context, it is worth mentioning that the magnetoelectric effect is expected to appear

in  $\text{LiFePO}_4$ , as also discussed in Reference [13]. The high magnetic field phase diagram was studied as well [14].

$^{57}\text{Fe}$  Mössbauer spectroscopy (MS) is capable of detecting very small hyperfine splitting due to the interactions of  $^{57}\text{Fe}$  nuclei with their surroundings. Such interactions comprise specific (static) electric and magnetic coupling of nuclei to electronic charge and spin distributions [15]. This makes MS of Fe sites/nuclei in  $\text{FeLiPO}_4$  a valuable tool to complement and check results of other techniques. For instance, magnetization measurements or neutron diffraction studies bring an “integral”/collective response from a sample measured. Moreover, it is certainly meaningful to inspect the sample from a “local” perspective obtained with Mössbauer spectroscopy (by accumulating resonant absorption events originating from individual nuclei). The main subject of the present study is thus low temperature magnetic properties as seen by Mössbauer spectroscopy and the way how MS can help in understanding aforementioned characteristics. Previous MS experimental investigations (see, e.g., References [16–18]) indicate that above  $T_N$  there is no magnetic ordering (only quadrupolar splitting is observed), whereas below  $T_N$  magnetic order is seen (magnetic hyperfine splitting is combined with the quadrupolar one). The question now arises: What happens if an external magnetic field is applied? Then, is the magnetic anisotropy large enough to prevent magnetic moments becoming aligned along the field?

Ab initio calculations may substantially help when answering such questions. The electronic structure, magnetic order and hyperfine interactions in  $\text{LiFePO}_4$  are examined computationally within the framework of the density functional theory (DFT) [19], assisting thereby the evaluation and interpretation of experimental MS data. Even if not all queries can be handled perfectly quantitatively, DFT-based approaches give usually valid responses with an unprecedented level of details, which is hard to obtain from experiment.

The paper is organized as follows. Section 2 describes experimental methods used, the studied  $\text{LiFePO}_4$  sample, and computational/theoretical approaches. In addition to Mössbauer experiments, the crystal structure and magnetic behavior of the sample are also examined. Section 3 then presents and discusses the obtained results, including the correlation between theory and experiment. The paper is concluded in Section 4, where also an outlook is given.

## 2. Experimental and Computational Methods

Figure 1 shows the orthorhombic structure of  $\text{LiFePO}_4$ . The corresponding space group is  $Pnma$  (standard setting, No. 62) [3]. This implies that the lattice parameter order is  $a > b > c$ , with the structure mirror planes perpendicular to the axis  $b$  (or [010] direction). These mirror planes (with  $y = 1/4, 3/4$ ) go through the Fe nuclei, which means the  $C_{1h}$  ( $C_s$ ) local point symmetry of Fe cations. The octahedral coordination of Fe cations (nominally 2+ charge) is also exhibited in Figure 1, where Fe atomic positions are numbered Fe1, Fe2, Fe3, and Fe4. We note that these Fe positions are all crystallographically equivalent (Wyckoff position 4c). Concerning magnetic order (occurring below  $T_N$ ), MMs at Fe1 and Fe3 sites are parallel, as well as those at Fe2 and Fe4. But MMs at the first group of sites are antiparallel to those at the second group of sites, if a small noncollinearity with the crystallographic axis  $b$  is neglected (see Reference [13] for details). Effectively, there are alternating Fe ion planes ( $y = 1/4$  and  $3/4$ ) with opposite MM directions collinear with  $b$ . At the same time, these planes represent mirrors of the  $\text{LiFePO}_4$  crystal.

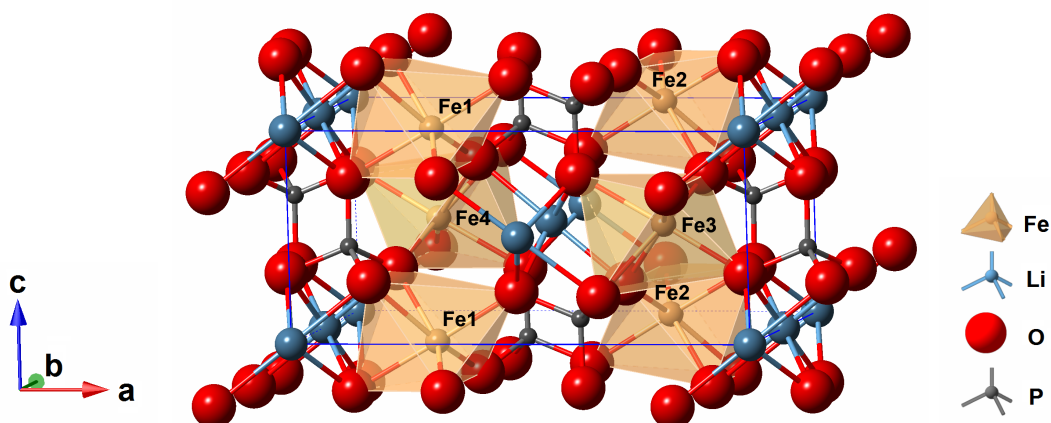


**Figure 1.** The crystal structure of  $\text{LiFePO}_4$ . The unit cell is indicated by blue lines. Fe coordination octahedra are also displayed. Fe atomic sites are denoted as Fe1, Fe2, Fe3, and Fe4 (there are two atoms shown for Fe1 and Fe2 atomic sites because of unit cell translation periodicity).

A powder sample obtained from Sigma-Aldrich (Product No. 759546) was studied. The particle size was smaller than  $5 \mu\text{m}$  (BET) and the sample purity was better than 97% (XRF). During the measurements, the powder particles were fixed using instant glue (solid polymer matrix). In order to check the crystal structure of the sample and find out the corresponding lattice parameters, X-ray diffraction (XRD) measurements were carried out. For this purpose, a Panalytical Empyrean diffractometer equipped with a Mo anode (wavelength  $\lambda = 0.70932 \text{ \AA}$ ) working in the parafocusing Bragg-Brentano geometry was employed. The diffractometer was furnished with a planar multilayer mirror in the primary beam and axial divergence eliminating Soller slit collimators with an acceptance of 0.02 rad in both the primary and diffracted beams. The diffracted intensity was detected with a 2D hybrid pixel single photon counting detector Galipix equipped with CdTe chip. Measured data were processed using the full powder pattern fitting procedure—Rietveld method. The computer program MStruct [20] was used for the fitting. The magnetic behavior of the studied sample at low temperatures represents also an important aspect in the current investigations. Magnetic properties of the powder  $\text{LiFePO}_4$  sample were examined using a Quantum Design superconducting quantum interference device MPMS XL 7T in fields up to 7 T and temperatures down to 2 K.

The  $^{57}\text{Fe}$  Mössbauer spectra of the sample were collected in transmission geometry using a constant-acceleration spectrometer with a  $^{57}\text{Co}/\text{Rh}$  source. The calibration of the spectrometer and determination of isomer shifts are given with respect to room temperature Mössbauer spectrum of  $\alpha$ -Fe foil. The Mössbauer spectra were acquired in a Janis bath cryostat at temperatures  $T = 60 \text{ K}$  and  $T = 4.2 \text{ K}$ . The in-field spectrum was received at 4.2 K in the external magnetic field  $B_{\text{ext}} = 6 \text{ T}$  oriented perpendicularly to the direction of the  $\gamma$ -rays. Measured spectra were evaluated using the current version of MossWinn<sup>®</sup> fitting programme [21]. The spectra at liquid helium temperature were analyzed by a procedure that makes use of the diagonalization of the full (static) hyperfine interaction Hamiltonian to calculate the relevant energy levels and the transition probabilities between these levels for the  $^{57}\text{Fe}$  isotope, assuming a random powder absorber. The following hyperfine parameters entering the Hamiltonian can, in principle, be extracted from measured Mössbauer  $^{57}\text{Fe}$  spectra: hyperfine magnetic field ( $B_{\text{hf}}$ ), originating mainly from the Fermi contact interaction, and electric field gradient (EFG) characterized by its principal tensor components  $V_{xx}$ ,  $V_{yy}$ , and  $V_{zz}$  (with the increasing magnitude), due to aspherical charge distribution around nucleus. If the EFG asymmetry is defined as  $\eta = (V_{xx} - V_{yy})/V_{zz}$ , the quadrupole splitting of the  $^{57}\text{Fe}$  nucleus translates into the EFG via the relation  $QS = eQV_{zz}\sqrt{1 + \eta^2/3}/2$  ( $e$  and  $Q$

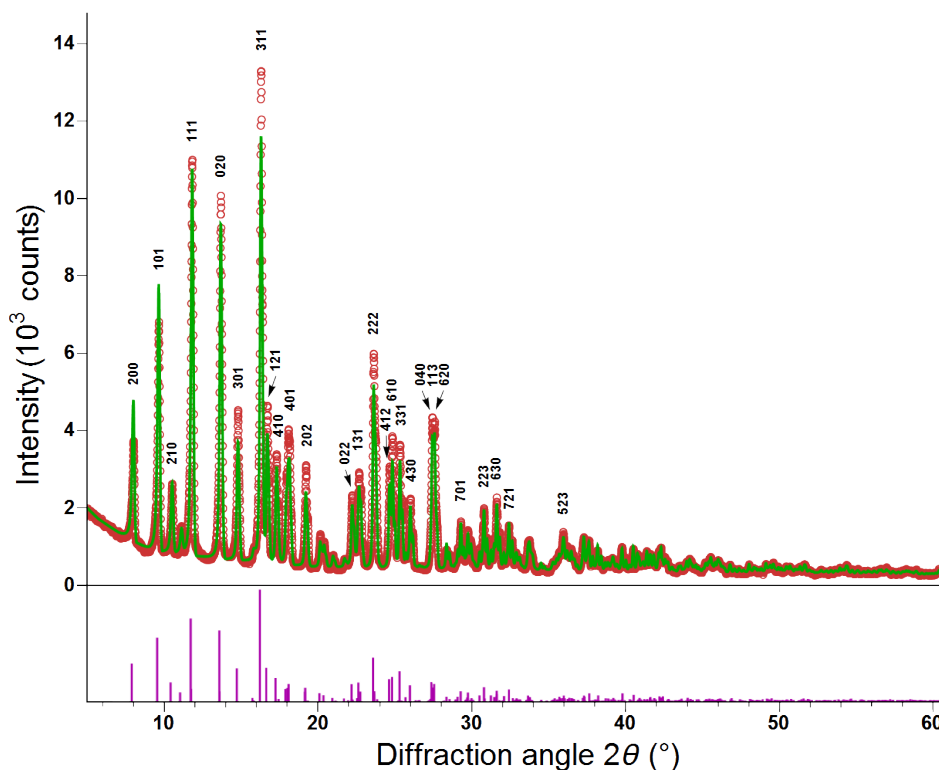
being the elementary charge and nuclear quadrupole moment, respectively). The quadrupole moment of the excited  $^{57}\text{Fe}$  nucleus was taken from Reference [22] to be  $Q = 0.16$  barn. If an external magnetic field ( $\mathbf{B}_{\text{ext}}$ ) is applied, then it sums up with  $\mathbf{B}_{\text{hf}}$  in the vectorial way, i.e., one gets an effective magnetic field  $B_{\text{eff}} = |\mathbf{B}_{\text{eff}}| = |\mathbf{B}_{\text{hf}} + \mathbf{B}_{\text{ext}}|$ , which determines the overall magnetic splitting of the  $^{57}\text{Fe}$  nuclear levels. For powder samples,  $\Delta B_{\text{eff}}$ , the distribution width of the effective magnetic field, is another useful parameter to characterize Mössbauer spectra. When such spectra are fitted, it is yet important to obtain the geometrical relationship of  $\mathbf{B}_{\text{eff}}$  or  $\mathbf{B}_{\text{hf}}$  and the EFG tensor. This relationship is defined using the parameter  $\theta$ , the polar angle between the direction of  $\mathbf{B}_{\text{eff}}$  and the principal axis of the main component  $V_{zz}$  of the EFG, and parameter  $\phi$ , the azimuthal angle between  $\mathbf{B}_{\text{eff}}$  and the  $V_{xx}$ 's principal axis. Finally, the isomer shift,  $IS$ , characterizes the change of the  $^{57}\text{Fe}$  nucleus' chemical environment with respect to a pure  $\alpha$ -iron sample. A negligible spectral component with an intensity of  $\sim 1\%$  corresponding likely to  $\text{Fe}^{3+}$  ions was subtracted from the measured spectra. This component can be due to a minor content of other phases and/or presence of point defects (in the vicinity of Fe ions, misplaced Fe ions, e.g., at Li sites) [23]. The origin of this spectral component will be studied in the future. The subtraction of the component does not affect the current evaluation of the magnetic structure in powdered  $\text{LiFePO}_4$ .

In order to calculate hyperfine parameters that are related to the electronic and magnetic structure of the studied material, a DFT-based approach was employed. In particular, the WIEN2k code [24], which is an implementation of the augmented plane wave plus local orbital [25,26] concept for electronic structure calculations for crystalline solids. In the course of calculations, the spin-polarized exchange-correlation functional—within the generalized gradient approximation [27]—after Perdew, Burke and Ernzerhof (PBE) [28] is used. The spin-orbit coupling (SOC) is also taken into account in specific investigations. The WIEN2k implementation is described in Reference [29], though in the present study the  $p_{1/2}$  local orbitals were not considered in SOC calculations. The calculations of the EFG and magnetic hyperfine field follows References [30,31] and [32,33], respectively.

### 3. Results and Discussion

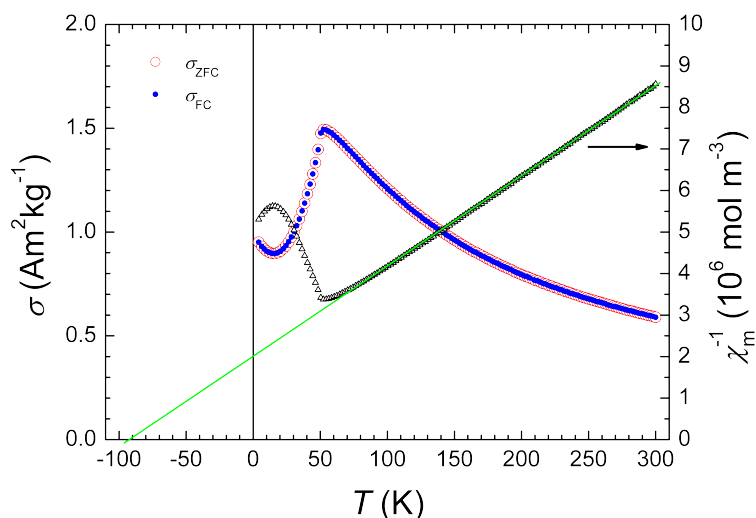
#### 3.1. Structural and Magnetic Measurements

Figure 2 shows the XRD patterns of the  $\text{LiFePO}_4$  sample. According to the powder XRD Rietveld analysis, the sample was assigned to be a single phase of an orthorhombic symmetry with the space group  $Pnma$  (No. 62). The observed lattice parameters  $a = 10.3234(3)$  Å,  $b = 6.0045(2)$  Å and  $c = 4.6915(1)$  Å are in a good agreement with the previous data [1,3,34,35] summarized also in Reference [2]. In this way, the expected structure of the investigated sample was confirmed. Moreover, we can infer that the Li stoichiometry of the sample is likely good since reduced Li content results in a decrease of the parameters  $a$  and  $b$  and an increase of the parameter  $c$ .



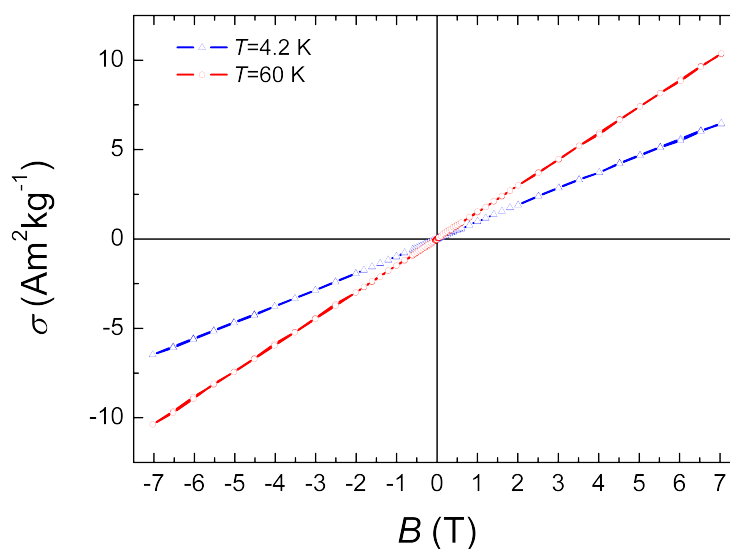
**Figure 2.** The XRD patterns of the  $\text{LiFePO}_4$  sample at room temperature. Experimental points are represented by red circles, whereas the green curve shows the fitted spectrum. Main peak indices are also given along with the peak positions (bottom part of the figure).

Figure 3 displays the temperature dependences of the zero field cooled (ZFC) and the field cooled (FC) magnetizations,  $\sigma_{(Z)FC}$ , under an applied magnetic field of 1 T. The results show a typical antiferromagnetic transition at  $T_N = 52$  K and a decrease in the magnetization with the decreasing temperature below  $T_N$ . For temperatures  $T > T_N$ , the molar susceptibility,  $\chi_m$ , see Figure 3, was fitted to the Curie-Weiss law  $\chi_m = C/(T + \Theta)$ ;  $C$  and  $\Theta$  are constants related to the measured system ( $\text{LiFePO}_4$ ) and observed magnetic phase transition. The Curie constant  $C = \mu_0 N_A \mu_{\text{eff}}^2 / 3k_B$ , with  $\mu_0$  being the vacuum permeability,  $N_A$  the Avogadro constant,  $k_B$  the Boltzmann constant, and  $\mu_{\text{eff}}$  the effective magnetic moment. The fitted values are  $\Theta = -91(2)$  K and  $C = 4.6(1) \times 10^{-5} \text{ m}^3\text{K/mol}$ . From the Curie constant  $C$ , the value  $\mu_{\text{eff}} = 5.5(1)$  Bohr magnetons ( $\mu_B$ ) is obtained, in good agreement with  $\Theta = -92(1)$  K and  $\mu_{\text{eff}} = 5.58(1) \mu_B$  reported in Reference [36] (see also Reference [17]). The effective magnetic moment is slightly higher than  $\mu_{\text{eff}} = 4.90 \mu_B$  for  $\text{Fe}^{2+}$  in the high-spin state ( $S = 2$ ) with the orbital angular momentum quenched ( $L \approx 0$ ) by the crystal field. The theoretical value of the high spin state of the free  $\text{Fe}^{2+}$  ion ( $S = 2, L = 2$ ) is  $\mu_{\text{eff}} = 6.71 \mu_B$ . A higher value of  $\mu_{\text{eff}}$  observed here thus indicates that the orbital angular momentum was not fully quenched by the crystal field. This observation is consistent with a non-zero orbital  $\text{Fe}^{2+}$  magnetic moment deduced from ab initio calculations discussed below. We mention an increase of the magnetization below temperature  $\sim 17$  K (Figure 3). Such an increase of the magnetization in  $\text{LiFePO}_4$  has also been reported in References [14,17,36]. Rhee et al. [17] related this effect to the influence of the spin-orbit coupling when it becomes comparable with the thermal energy at about 20 K, which results in an ‘unquenching’ of the orbital magnetic moments of  $\text{Fe}^{2+}$  ions, thus increasing their total magnetic moment.



**Figure 3.** Temperature dependences of the  $\sigma_{ZFC}$  (zero field cooled—open circles),  $\sigma_{FC}$  (field cooled—solid circles) magnetization and inverse molar susceptibility  $\chi_m^{-1}$  (open triangles) of the  $\text{LiFePO}_4$  sample at the magnetic field 1 T.

The magnetization curves of the  $\text{LiFePO}_4$  sample were measured at temperatures 4.2 K and 60 K and are presented in Figure 4. A linear dependence of the magnetic moment on the magnetic field typical for an AF material was observed at the liquid helium temperature. A larger value of the magnetic moment at 60 K is due to the transition from the AF to the paramagnetic state, which is clearly seen in the temperature dependence of the magnetization in a field of 1 T (Figure 3). We can state that the AF character of the magnetic order in the studied  $\text{LiFePO}_4$  sample is confirmed by the magnetic measurements discussed above, and we can take it into account in the subsequent analysis of the Mössbauer spectra.



**Figure 4.** The magnetization curves of the  $\text{LiFePO}_4$  sample measured at temperatures 4.2 K and 60 K.

### 3.2. Mössbauer Spectroscopy of LiFePO<sub>4</sub>

Mössbauer spectra were collected and evaluated for three different experimental conditions varying in temperature and external magnetic field: (i)  $T = 60$  K ( $> T_N$ ),  $B_{\text{ext}} = 0$  T; (ii)  $T = 4.2$  K ( $< T_N$ ),  $B_{\text{ext}} = 0$  T; and (iii)  $T = 4.2$  K ( $< T_N$ ),  $B_{\text{ext}} = 6$  T. The fitted parameters of the spectra are shown in Table 1 and discussed in detail below. The overall observation is that theory—as discussed in more detail the subsequent section—underestimates the  $V_{zz}$  and  $\eta$  parameters and overestimates  $B_{\text{hf}}$  (when only the Fermi contact interaction contributes to  $B_{\text{hf}}$ ).

**Table 1.** The hyperfine parameters determined from the <sup>57</sup>Fe Mössbauer spectra in LiFePO<sub>4</sub> for the three experiments performed.  $I$  stands for the intensity of spectral components. Underlined numbers represent the mean values of corresponding quantities. In the case of  $B_{\text{hf}}$  ( $B_{\text{ext}} = 6$  T), the value is in fact the mean value of  $B_{\text{eff}}$ . Whereas for  $B_{\text{ext}} = 0$  T ( $T = 4.2$  K), it is not necessary to consider the value as an average since the distribution width is very small.

Spectrum Type	$T$ (K)	$B_{\text{ext}}$ (T)	$B_{\text{hf}}$ (T)	$IS$ (mm/s)	$QS$ (mm/s)	$I$ (%)	$\Gamma$ (mm/s)	$V_{zz}$ (10 <sup>21</sup> V/m <sup>2</sup> )	$\eta$	$\phi$ (°)	$\vartheta$ (°)	$\Delta B_{\text{eff}}$ (T)
D	60	0	–	1.33(2)	3.01(2)	100	0.30(1)	–	–	–	–	–
O	4.2	0	12.4(2)	1.35(2)	3.05(2)	100	0.29(1)	16.7	0.77(1)	0	0	~0.3
O	4.2	6	<u>12.7</u> (2)	1.35(2)	3.04(2)	100	0.29(1)	16.7	0.78(1)	<u>~143</u>	<u>~13</u>	~6

The <sup>57</sup>Fe Mössbauer spectrum of LiFePO<sub>4</sub> above the Néel temperature at temperature  $T = 60$  K, see Figure 5, was fitted with a symmetrical, Lorentzian-shaped quadrupole doublet D. The doublet D with reasonably narrow line widths  $\Gamma = 0.30(1)$  mm/s, quadrupole splitting  $QS = 3.02(2)$  mm/s and isomer shift  $IS = 1.33(2)$  mm/s (in agreement with work [16]), see Table 1, was assigned to ferrous Fe<sup>2+</sup> ions in the high spin state  $S = 2$  [15,37].

At temperature  $T = 4.2$  K the <sup>57</sup>Fe Mössbauer spectrum was fitted with one octet O (eight absorption lines [38]) with a narrow distribution of  $B_{\text{hf}}$  in the static Hamiltonian (see Figure 6). The octet component O with  $B_{\text{hf}} = 12.4(2)$  T,  $QS = 3.05(2)$  mm/s, and  $IS = 1.35(2)$  mm/s were ascribed, similarly to the doublet D at  $T = 60$  K, to Fe<sup>2+</sup> ions with the high spin state  $S = 2$ . The orientation of  $B_{\text{hf}}$  on <sup>57</sup>Fe nuclei is antiparallel to the orientation of the magnetic moment of Fe<sup>2+</sup> ions (like in pure iron), which is parallel to the crystallographic direction [010] [10]. The principal axis of the EFG main component  $V_{zz} = 16.7(1) \times 10^{21}$  V/m<sup>2</sup>, with respect to the zero polar angle  $\vartheta \sim 0^\circ$ , see Table 1, is collinear with the direction [010], which is expectable in some respect (because of the Fe site symmetry, one principal EFG axis should be parallel with this direction). At the Fe<sup>2+</sup> sites, due to a non-zero value of the asymmetry parameter  $\eta \sim 0.8$ , there is no ordinary local symmetry axis, except the normal to the mirror plane (i.e., C<sub>1h</sub> point symmetry).

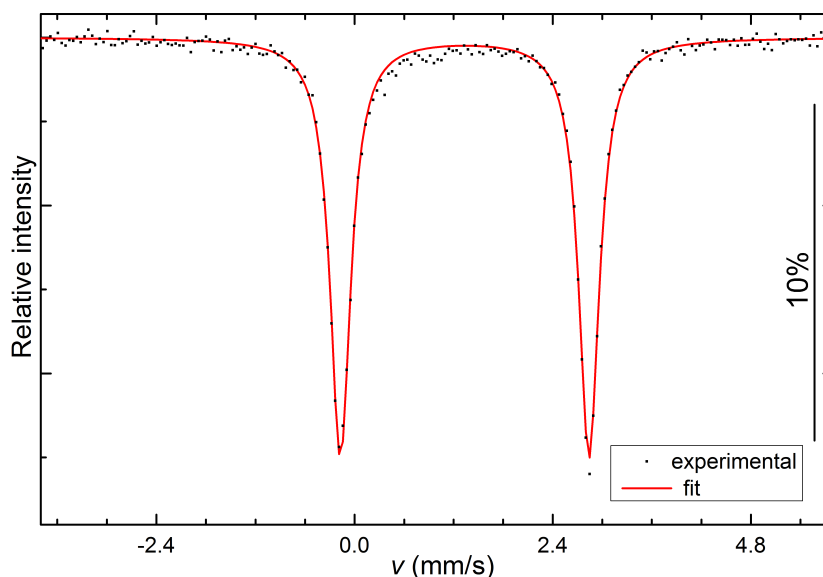


Figure 5. The  $^{57}\text{Fe}$  Mössbauer spectrum of  $\text{LiFePO}_4$  above Néel temperature at  $T = 60$  K.

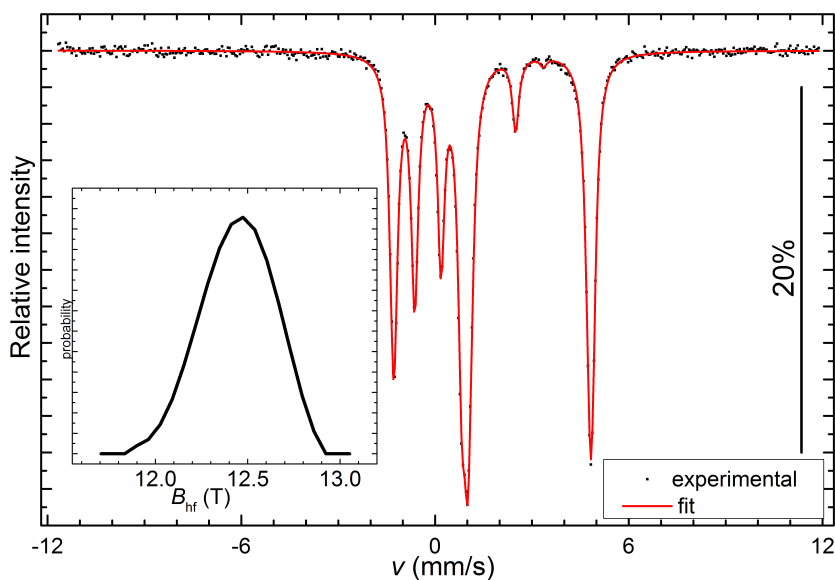
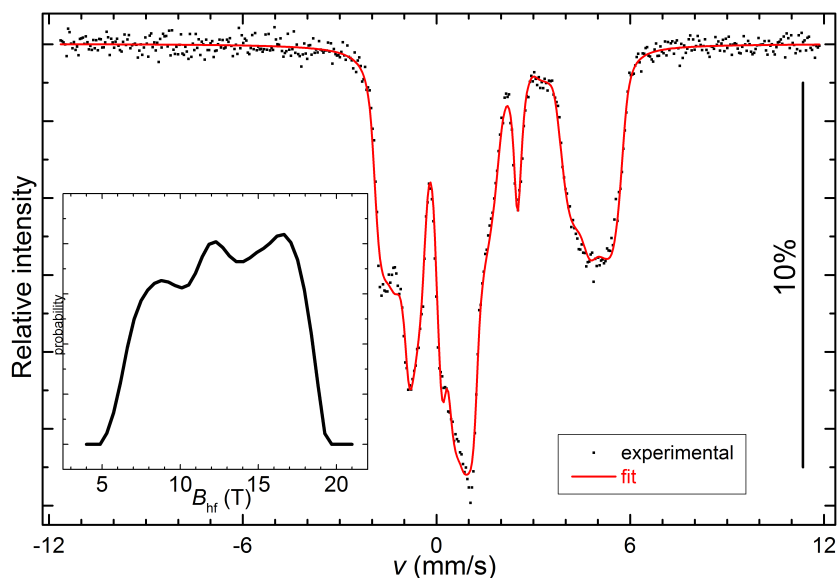


Figure 6. The  $^{57}\text{Fe}$  Mössbauer spectrum of  $\text{LiFePO}_4$  at liquid helium temperature ( $T = 4.2$  K,  $B_{\text{ext}} = 0$  T). The inset shows the distribution of  $B_{\text{hf}}$  at the nuclei.

The in-field Mössbauer spectrum of  $\text{LiFePO}_4$  at  $T = 4.2$  K and  $B_{\text{ext}} = 6$  T is presented in Figure 7. The application of the external field provokes a broadening of the octet O lines due to the vectorial sum of randomly oriented local  $B_{\text{hf}}$  and the applied external field  $B_{\text{ext}}$  perpendicular to the  $\gamma$ -ray direction. The average value of the polar angle  $\theta \sim 13^\circ$ , see Table 1, and a higher probability above the mean value of  $B_{\text{hf}}$ , see inset in Figure 7, indicates the canting of the  $\text{Fe}^{2+}$  moments arranged originally antiferromagnetically. In fact, there are four nonequivalent Fe ion sites with respect to hyperfine interactions when an external magnetic field is applied. Since the single Fe ion magnetic anisotropy is strong, which is explained below, the external field does not cause significant deviation of the Fe ion MM

from its original direction along [010], and in the fit we can consider just one Fe site where its MM is slightly deviated from [010], while  $B_{\text{eff}}$  possesses a broad distribution.



**Figure 7.** The  $^{57}\text{Fe}$  Mössbauer spectrum of  $\text{LiFePO}_4$  at temperature  $T = 4.2$  K and external magnetic field  $B_{\text{ext}} = 6$  T. The inset displays the distribution of  $B_{\text{eff}}$  at the  $^{57}\text{Fe}$  nuclei.

### 3.3. Theoretical Exploration of Magnetism and Hyperfine Interactions

The magnetic structure of LFP was deduced to be antiferromagnetic (AF)—as also confirmed here for the sample studied—with the easy magnetization axis along the [010] direction, based on neutron scattering experiments [9,10]. Other experiments [11–13] confirmed this finding, except small deviations from this direction due to anisotropic exchange, which is not taken into account in the following considerations. In addition to the easy magnetization direction, another question arises. Namely, what is the arrangement of the magnetic moments in the  $\text{LiFePO}_4$  unit cell? There are three possible MM orders which result in an AF order. These are: Fe1 and Fe2 MMs are parallel ( $\uparrow\uparrow$ ) being antiparallel ( $\uparrow\downarrow$ ) to  $\downarrow\downarrow$  Fe3 and Fe4 (AF1), (Fe1  $\uparrow\uparrow$  Fe3)  $\uparrow\downarrow$  (Fe2  $\downarrow\downarrow$  Fe4) (AF2), and (Fe1  $\uparrow\uparrow$  Fe4)  $\uparrow\downarrow$  (Fe2  $\downarrow\downarrow$  Fe3) (AF3). Our DFT PBE spin-polarized calculations (without SOC) show that the AF2 order exhibits the lowest energy, followed by AF1 and the highest energy occurs for AF3. In all calculations the lattice parameters from Reference [3], i.e.,  $a = 10.332$  Å,  $b = 6.010$  Å and  $c = 4.692$  Å, were employed. Table 2 collects results of these calculations (see the second column). The AF2 order is observed in reality (see, e.g., Reference [10]) and was also confirmed in other computations [8,18].

**Table 2.** Results of density functional theory (DFT) calculations for the three antiferromagnetic (AF) configurations. The first column indicates the AF configuration.  $\Delta E_{\text{AF}}$  is the unit cell total energy relative to the lowest energy configuration.  $B_{\text{hf}}$  covers the contact (isotropic) interaction only.

Order	$\Delta E_{\text{AF}}$ (meV)	$V_{\text{zz}}$ ( $10^{21}$ V/m $^2$ )	$\eta$	$B_{\text{hf}}$ (T)
AF1	35.9	14.2	0.61	32.7
AF2	00.0	14.1	0.63	32.8
AF3	65.1	13.1	0.55	31.4

Table 2 also contains results of hyperfine parameter calculations. One can see that  $B_{\text{hf}}$  is significantly overestimated (see Table 1 for comparison with experiment), which is likely the effect of neglecting other contributions to the hyperfine field, which will be yet discussed below (see also Reference [17]). The  $V_{zz}$  value is underestimated by about 15%, which is acceptable and a common feature when experimental and computational EFG results are related. The values of asymmetry parameter ( $\eta$ ) are also underestimated compared to experiment. AF1 and AF2 show very similar hyperfine parameters, whereas AF3 differs slightly from them. Nevertheless, this indicates a weak sensitivity of the EFG and Fermi contact contribution to  $B_{\text{hf}}$  to various antiferromagnetic arrangements (Reference [18] reports similar observation).

With regard to the evaluations of more complex experimental situations, we note that different Fe ions have generally different orientations of the EFG principal axes with respect to the lattice translation vectors. This fact is documented in Figure 8 where EFG axes are schematically shown for each of Fe1, Fe2, Fe3, and Fe4 ions together with the directions of translation vectors  $a$ ,  $b$ , and  $c$ . Thus, on one hand, Fe1 and Fe2 have the same EFG axis orientations, and, on the other hand, Fe3 and Fe4 have also the same orientations, but distinct from that of Fe1 and Fe2. The  $V_{zz}$  axis is always along  $b$ , and  $V_{yy}$  and  $V_{xx}$  axes are always in the  $a$ - $c$  plane, though they are tilted from the  $a$  and  $c$  directions. For  $B_{\text{ext}} = 0$ , all Fe ions are equivalent with respect to hyperfine interactions. When the external magnetic field is applied along  $b$ , EFG principal axis orientations are unimportant since  $\vartheta = 0^\circ$  [15]. In this case, Fe1 and Fe3 are pairwise equivalent as well as are Fe2 and Fe4, because of the “magnetic” equivalence within the AF2 order, as discussed above. Considering the most general situation, when  $B_{\text{ext}}$  is deviated from the easy magnetization axis  $b$ , results in the outcome that all Fe sites are nonequivalent regarding the hyperfine interactions.

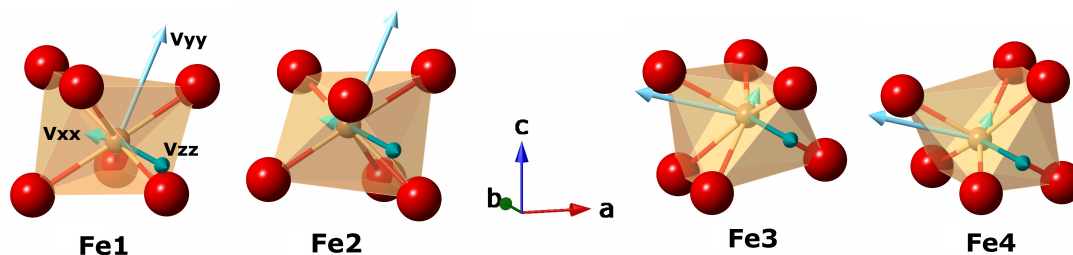


**Figure 8.** Electric field gradient (EFG) tensor principal axes for Fe1, Fe2, Fe3, and Fe4 cations (shown with their corresponding coordination octahedra; cf. Figure 1). Coloring of EFG  $V_{zz}$ ,  $V_{yy}$ , and  $V_{xx}$  axes/vectors is illustrated for the Fe1 case and kept identical for other cations. The length of vectors corresponds to the size of  $V_{zz}$ ,  $V_{yy}$ , and  $V_{xx}$  EFG tensor components.

When the SOC is enabled in the DFT calculations, it is possible to find the easy and hard magnetization directions. Table 3 lists results of three calculations with the magnetization kept collinear with  $a$ ,  $b$ , and  $c$  directions while retaining the AF2 order. The total energies per unit cell are given relative to the lowest energy in the second column. One can see that the easy magnetization direction is  $b$  ([010]), whereas  $c$  ([001]) appears to be the hard direction. The  $a$  ([100]) magnetization direction is somewhat softer than the previous one. This is in good agreement with experimental observations [13]. The spin magnetic moment of Fe ions calculated in the muffin-tin sphere is  $3.49 \mu_B$ , which is reasonable considering that no correction to account for correlated  $3d$ -electrons of Fe was applied (cf., e.g., Reference [39]). The orbital contributions ( $m_l$ ) to the magnetic moment are also given in Table 3 for all three investigated cases (magnitude is shown only). The largest contribution  $0.11 \mu_B$  occurs for the easy magnetization direction. When the energy difference (per Fe ion) between the hard and soft direction is compared to the energy of the  $\text{Fe}^{2+}$  ion with a magnetic moment of  $4 \mu_B$  in the magnetic field  $B_{\text{ext}}$ , one gets that these energies match at the field  $B_{\text{ext}} \simeq 40$  T. Then, a significant deviation from the easy magnetization direction may happen only when

$B_{\text{ext}}$  approaches 40 T, demonstrating a large single ion magnetic anisotropy of Fe ions in  $\text{LiFePO}_4$ . This is consistent with the in-field MS results discussed above where a relatively small (average) deviation of the Fe ion MMs from the easy axis direction is observed at the field  $B_{\text{ext}} = 6$  T. Moreover, the above considerations about distinct hyperfine interactions at four Fe ion sites confirm the approach regarding how the corresponding MS spectrum was fitted.

**Table 3.** Results of easy/hard magnetization direction calculations with the spin-orbit coupling (SOC) taken into account. The first column indicates the direction with which Fe ion MMs are collinear.  $\Delta E_{\text{eh}}$  is the unit cell total energy relative to the easy direction case.  $B_{\text{hf}}$  also includes orbital and spin dipolar contributions.

MM	$\Delta E_{\text{eh}}$ (meV)	$V_{\text{zz}}$ ( $10^{21}$ V/m <sup>2</sup> )	$\eta$	$m_l$ ( $\mu_B$ )	$B_{\text{hf}}$ (T)
[100]	4.55	14.0	0.65	0.08	30.5
[010]	0.00	14.1	0.63	0.11	11.7
[001]	9.19	14.1	0.62	0.03	43.3

When coming to the hyperfine parameters, the EFG—characterized by  $V_{\text{zz}}$  and  $\eta$ —is almost not affected by switching on the SOC (cf. Table 2). On the other hand,  $B_{\text{hf}}$  is strongly affected and depends on the magnetization direction.  $B_{\text{hf}}$  values (see Table 3) now include the orbital magnetic moment and dipolar spin contributions [33] (whereas previous numbers originated from the Fermi contact interaction only). The value  $B_{\text{hf}} = 11.7$  T calculated for the magnetization direction collinear with the  $b$  axis ([010]) is now very close to the corresponding experimental value 12.4 T (see Table 1).

From these considerations, it becomes obvious that for an adequate description of magnetic hyperfine interactions it is necessary to include their anisotropy. A sufficiently general expression for the nuclear Hamiltonian could be written as

$$\hat{H}_{\text{hf}} = \langle \hat{S} \rangle \mathcal{A} \hat{I}, \quad (1)$$

where  $\hat{I}$  is the operator of the nuclear spin,  $\langle \hat{S} \rangle$  is the quantum-mechanical and thermodynamic mean value of the Fe ion spin operator, and  $\mathcal{A}$  is the second order tensor (matrix) describing such type of hyperfine interaction. In principle, each Fe ionic site may have different tensor  $\mathcal{A}$  in the global coordinate system, which is important in the case when an external magnetic field is applied. A possibly anisotropic (dipolar) contribution from other Fe sites to the hyperfine field should also be considered. Currently, the code [21] used to fit the Mössbauer spectra does not allow us to take into account anisotropic magnetic hyperfine interactions. In the case of an isotropic interaction, the tensor  $\mathcal{A}$  reduces to a constant  $A$ . When the nuclear magnetic moment operator is  $\hat{\mu} = g_N \mu_N \hat{I}$  ( $g_N$  and  $\mu_N$  being, respectively, the  $g$ -factor of the  $^{57}\text{Fe}$  nucleus and nuclear magneton),  $B_{\text{hf}} = -A \langle \hat{S} \rangle / (g_N \mu_N)$ . Since  $\langle \hat{S} \rangle$  is proportional to the ion magnetic moment, so is  $B_{\text{hf}}$ . An example of how to handle the anisotropic magnetic hyperfine interaction can be found in Reference [40] where iron phosphide ( $\text{FeP}$ ) having an orthorhombic structure with the same space group as  $\text{LiFePO}_4$  was investigated.  $B_{\text{hf}}$  values from Table 3 could be used to estimate the tensor  $\mathcal{A}$  (supposed for simplicity to be diagonal in the coordinate system with axes parallel to orthorhombic  $a$ ,  $b$ , and  $c$  translation vectors) considering that Fe ions are in the high spin state  $S = 2$  regardless of the magnetic moment orientation.

When studying magnetic anisotropy, the single ion anisotropy may play an important role in addition to the exchange interaction anisotropy. The general formula to describe the magnetic anisotropy energy originating from the individual atoms of a crystal reads

$$E_{\text{MA}}(\theta, \varphi) = \sum_i \sum_{l=0}^{\infty} \sum_{m=-l}^l K_{lm}^{(i)} Y_{lm}(\theta, \varphi), \quad (2)$$

with  $K_{lm}^{(i)}$  being the anisotropy constants of  $i$ -th atom/ion and  $Y_{lm}$  are spherical harmonics expressed in terms of spherical coordinates ( $\theta$  polar and  $\varphi$  azimuthal angle [41]). The summation over atoms goes through all atoms contributing to the anisotropy. Since atomic sites have usually some non trivial symmetry, the effective number of anisotropy constants is reduced. The summation over  $l$  is typically limited by 2, 4, or 6.

Using the work [42] and the so-called real spherical harmonics, we can deduce the formula describing magnetocrystalline anisotropy (up to  $l = 2$ ) per one Fe atom reflecting its  $C_{1h}$  (mirror) point symmetry in LiFePO<sub>4</sub>:

$$E_{\text{MA}}^{(1)}(\theta, \varphi) = K_{00} + K_{11c} \sin \theta \cos \varphi + K_{11s} \sin \theta \sin \varphi + K_{20} \cos^2 \theta + K_{22c} \sin^2 \theta \cos 2\varphi + K_{22s} \sin^2 \theta \sin 2\varphi, \quad (3)$$

where  $K_{lm[c/s]}$  are anisotropy constants and  $\theta, \varphi$  are defined with respect to a suitable coordinate system. Namely,  $\theta$  is the deviation from the axis  $\mathbf{b}$ , whereas  $\varphi$  does not need to be fixed at this moment. Equation (3) is valid for one Fe ion. We have, however, same equations for other ions where anisotropy constants are the same, but  $\theta$  and  $\varphi$  angles are related using symmetry operations (rotations) which mutually transform Fe ion surroundings. In this way, there are just 6 anisotropy constants. They could, in principle, be obtained using ab initio calculations by taking into account the spin-orbit coupling. By considering the external magnetic field and single ion magnetic anisotropy, the direction of MMs at individual Fe sites can be determined. This may serve as a starting point to fit more precisely Mössbauer spectra considering also the anisotropic magnetic hyperfine interaction and EFG tensor principal axis geometrical relationships discussed above.

#### 4. Conclusions and Outlook

The LiFePO<sub>4</sub> powder sample was first examined experimentally. Its crystal structure at room temperature and magnetic order below the Néel temperature were determined, demonstrating a fair agreement with previous investigations. The Mössbauer study of this LiFePO<sub>4</sub> sample was then performed, showing the good potential of this technique to investigate complex magnetic structures. Measurements done above and below the Néel temperature agree with earlier Mössbauer studies. A doublet and an octet are detected, respectively, in the corresponding spectra. Applying an external magnetic field to the sample at liquid helium temperature results in the deviations of Fe magnetic moments from the crystallographic axis  $\mathbf{b}$ , being the easy magnetization direction. A small average size of such deviations points to a strong magnetic anisotropy. Moreover, a rather flat distribution of the magnetic effective fields ranging from about 6 to 19 T shows that the external field is added to or subtracted from the hyperfine field, indicating again a large anisotropy. Whereas the distribution should be narrow and peaked at about 6.5 T when the anisotropy is weak—magnetic moments follow the external field, thus destroying the antiferromagnetic order, which was not observed.

By studying theoretically/computationally various features of the magnetic order and hyperfine interactions in LiFePO<sub>4</sub>, we may state a good predictability of experimental results and suggest an advanced method of Mössbauer spectra evaluations, preferably from measurements carried out for single crystal specimens. It is observed that in addition to the Fermi contact term, the orbital magnetic moments of Fe ions contribute significantly to the hyperfine field. The spin-dipolar contribution is important too. The single Fe ion anisotropy is predicted to be high in agreement with experiment. An expression describing the single ion magnetic anisotropy is suggested and its parameters could be obtained in the future by means of SOC DFT calculations with varying directions of the magnetization. This would allow us to determine the direction of magnetic moments at individual Fe sites upon application of the magnetic field, which can be used to fit the Mössbauer spectra more adequately.

**Author Contributions:** Conceptualization and methodology, T.K., J.K. (Jaroslav Kohout) and J.K. (Jan Kuriplach); measurements and data evaluations, T.K., J.K. (Jaroslav Kohout), M.D., and M.V.; computations and formal analysis, J.Ku.; writing—review and editing, T.K., J.K. (Jaroslav Kohout) and J.K. (Jan Kuriplach).

**Funding:** The support by projects SVV-2017-260442 and NanoCent—Nanomaterials Centre for Advanced Applications, project No. CZ.02.1.01/0.0/0.0/15\_003/0000485, financed by ERDF, is gratefully acknowledged. Magnetic experiments were performed in MGML—Materials Growth & Measurement Laboratory (<http://www.mgml.eu>), which is supported within the program of Czech Research Infrastructures (project No. LM2018096). Jan Kuriplach was partially supported by the Czech Republic’s Ministry of Education, Youth and Sports from the Large Infrastructures for Research, Experimental Development and Innovations project “IT4Innovations National Supercomputing Center—LM2015070”.

**Acknowledgments:** Fruitful discussions with B. Barbiellini are appreciated. The authors gratefully acknowledge K. Závěta for his advices and help concerning the interpretation of magnetic measurements. Figures related to the visualization of the LiFePO<sub>4</sub> crystal structure were generated using CrystalMaker®. CrystalMaker Software Ltd., Oxford, England (<http://www.crystallmaker.com>).

**Conflicts of Interest:** The authors declare no conflict of interest.

## References and Notes

1. Padhi, A.K.; Nanjundaswamy, K.S.; Goodenough, J.B. Phospho-olivines as Positive-Electrode Materials for Rechargeable Lithium Batteries. *J. Electrochem. Soc.* **1997**, *144*, 1188–1194. [[CrossRef](#)]
2. Mauger, A.; Julien, C.M. Olivine Positive Electrodes for Li-Ion Batteries: Status and Perspectives. *Batteries* **2018**, *4*, 39. [[CrossRef](#)]
3. Streltsov, V.A.; Belokoneva, E.L.; Tsirelson, V.G.; Hansen, N.K. Multipole analysis of the electron density in triphylite, LiFePO<sub>4</sub>, using X-ray diffraction data. *Acta Cryst. B* **1993**, *49*, 147–153. [[CrossRef](#)]
4. Liu, C.; Neale, Z.G.; Cao, G. Understanding electrochemical potentials of cathode materials in rechargeable batteries. *Mater. Today* **2016**, *19*, 109–123. [[CrossRef](#)]
5. Liu, X.; Wang, Y.J.; Barbiellini, B.; Hafiz, H.; Basak, S.; Liu, J.; Richardson, T.; Shu, G.; Chou, F.; Weng, T.C.; et al. Why LiFePO<sub>4</sub> is a safe battery electrode: Coulomb repulsion induced electron-state reshuffling upon lithiation. *Phys. Chem. Chem. Phys.* **2015**, *17*, 26369–26377. [[CrossRef](#)] [[PubMed](#)]
6. Kuriplach, J.; Pulkkinen, A.; Barbiellini, B. First principles study of the impact of grain boundary formation in the cathode material LiFePO<sub>4</sub>. *Condens. Matter* **2019**, *4*, 80. [[CrossRef](#)]
7. Lachal, M.; Bouchet, R.; Boulineau, A.; Surblé, S.; Rossignol, C.; Alloin, F.; Obbade, S. Remarkable impact of grains boundaries on the chemical delithiation kinetics of LiFePO<sub>4</sub>. *Solid State Ion.* **2017**, *300*, 187–194. [[CrossRef](#)]
8. Jena, A.; Nanda, B.R.K. Unconventional magnetism and band gap formation in LiFePO<sub>4</sub>: Consequence of polyanion induced non-planarity. *Sci. Rep.* **2016**, *6*, 19573. [[CrossRef](#)]
9. Santoro, R.P.; Newnham, R.E. Antiferromagnetism in LiFePO<sub>4</sub>. *Acta Cryst.* **1967**, *22*, 344–347. [[CrossRef](#)]
10. Rousse, G.; Rodriguez-Carvajal, J.; Patoux, S.; Masquelier, C. Magnetic structures of the triphylite LiFePO<sub>4</sub> and of its delithiated form FePO<sub>4</sub>. *Chem. Mater.* **2003**, *15*, 4082–4090. [[CrossRef](#)]
11. Li, J.; Garlea, V.O.; Zarestky, J.L.; Vakhnin, D. Spin-waves in antiferromagnetic single-crystal LiFePO<sub>4</sub>. *Phys. Rev. B* **2006**, *73*, 024410. [[CrossRef](#)]
12. Liang, G.; Park, K.; Li, J.; Benson, R.E.; Vakhnin, D.; Markert, J.T.; Croft, M.C. Anisotropy in magnetic properties and electronic structure of single-crystal LiFePO<sub>4</sub>. *Phys. Rev. B* **2008**, *77*, 064414. [[CrossRef](#)]
13. Toft-Petersen, R.; Reehuis, M.; Jensen, T.B.S.; Andersen, N.H.; Li, J.; Le, M.D.; Laver, M.; Niedermayer, C.; Klemke, B.; Lefmann, K.; et al. Anomalous magnetic structure and spin dynamics in magnetoelectric LiFePO<sub>4</sub>. *Phys. Rev. B* **2015**, *92*, 024404. [[CrossRef](#)]
14. Werner, J.; Sauerland, S.; Koo, C.; Neef, C.; Pollithy, A.; Skourski, Y.; Klingeler, R. High magnetic field phase diagram and failure of the magnetic Grüneisen scaling in LiFePO<sub>4</sub>. *Phys. Rev. B* **2019**, *99*, 214432. [[CrossRef](#)]
15. Gütllich, P.; Bill, E.; Trautwein, A.X. *Mössbauer Spectroscopy and Transition Metal Chemistry. Fundamentals and Applications*; Springer: Berlin/Heidelberg, Germany, 2011. [[CrossRef](#)]
16. Van Alboom, A.; De Grave, E.; Wohlfahrt-Mehrens, M. Temperature dependence of the Fe<sup>2+</sup> Mössbauer parameters in triphylite (LiFePO<sub>4</sub>). *Am. Mineral.* **2011**, *96*, 408–416. [[CrossRef](#)]

17. Rhee, C.H.; Lee, I.K.; Moon, S.J.; Kim, S.J.; Kim, C.S. Neutron diffraction and Mössbauer studies of LiFePO<sub>4</sub>. *J. Korean Phys. Soc.* **2011**, *58*, 472–475. [CrossRef]
18. El Khalifi, M.; Lippens, P.E. First-principles investigation of the <sup>57</sup>Fe Mössbauer parameters of LiFePO<sub>4</sub> and FePO<sub>4</sub>. *J. Phys. Chem. C* **2016**, *120*, 28375–28389. [CrossRef]
19. Hohenberg, P.; Kohn, W. Inhomogeneous electron gas. *Phys. Rev.* **1964**, *136*, B864–B871. [CrossRef]
20. Matěj, Z.; Kužel, R.; Nichtová, L. XRD total pattern fitting applied to study of microstructure of TiO<sub>2</sub> films. *Powder Diffr.* **2010**, *25*, 125–131. [CrossRef]
21. Klencsár, Z.; Kuzmann, E.; Vértés, A. User-friendly software for Mössbauer spectrum analysis. *J. Radioanal. Nucl. Chem.* **1996**, *210*, 105–118. [CrossRef]
22. Dufek, P.; Blaha, P.; Schwarz, K. Determination of the nuclear quadrupole moment of <sup>57</sup>Fe. *Phys. Rev. Lett.* **1995**, *75*, 3545–3548. [CrossRef] [PubMed]
23. Hamelet, S.; Gibot, P.; Casas-Cabanas, M.; Bonnin, D.; Grey, C.P.; Cabana, J.; Leriche, J.B.; Rodriguez-Carvajal, J.; Courty, M.; Lvasseur, S.; et al. The effects of moderate thermal treatments under air on LiFePO<sub>4</sub>-based nano powders. *J. Mater. Chem.* **2009**, *19*, 3979–3991. [CrossRef]
24. Blaha, P.; Schwarz, K.; Madsen, G.K.H.; Kvasnicka, D.; Luitz, J.; Laskowski, R.; Tran, F.; Marks, L.D. *WIEN2k, An Augmented Plane Wave + Local Orbitals Program for Calculating Crystal Properties*; Karlheinz Schwarz, Technische Universität Wien: Wien, Austria, 2001; ISBN 3-9501031-1-2.
25. Singh, D. Ground-state properties of lanthanum: Treatment of extended-core states. *Phys. Rev. B* **1991**, *43*, 6388–6392. [CrossRef] [PubMed]
26. Schwarz, K.; Blaha, P.; Madsen, G.K.H. Electronic structure calculations of solids using the WIEN2k package for material sciences. *Comp. Phys. Commun.* **2002**, *147*, 71–76. [CrossRef]
27. Perdew, J.P.; Chevary, J.A.; Vosko, S.H.; Jackson, K.A.; Pederson, M.R.; Singh, D.J.; Fiolhais, C. Atoms, molecules, solids, and surfaces: Applications of the generalized gradient approximation for exchange and correlation. *Phys. Rev. B* **1992**, *46*, 6671–6687. [CrossRef]
28. Perdew, J.P.; Burke, K.; Ernzerhof, M. Generalized gradient approximation made simple. *Phys. Rev. Lett.* **1996**, *77*, 3865–3868. [CrossRef]
29. Kuneš, J.; Novák, P.; Schmid, R.; Blaha, P.; Schwarz, K. Electronic structure of fcc Th: Spin-orbit calculation with 6p<sub>1/2</sub> local orbital extension. *Phys. Rev. B* **2001**, *64*, 153102. [CrossRef]
30. Blaha, P.; Schwarz, K.; Herzig, P. First-principles calculation of the electric field gradient of Li<sub>3</sub>N. *Phys. Rev. Lett.* **1985**, *54*, 1192–1195. [CrossRef]
31. Singh, D.J.; Schwarz, K.; Blaha, P. Electric-field gradients in YBa<sub>2</sub>Cu<sub>3</sub>O<sub>7</sub>: Discrepancy between experimental and local-density-approximation charge distributions. *Phys. Rev. B* **1992**, *46*, 5849–5852. [CrossRef]
32. Blügel, S.; Akai, H.; Zeller, R.; Dederichs, P.H. Hyperfine fields of 3d and 4d impurities in nickel. *Phys. Rev. B* **1987**, *35*, 3271–3283. [CrossRef]
33. Novák, P. *Calculation of Hyperfine Field in WIEN2k*; Technical Report; Technische Universität Wien: Wien, Austria, 2006. Available online: [http://www.wien2k.at/reg\\_user/textbooks/Bhf\\_3.pdf](http://www.wien2k.at/reg_user/textbooks/Bhf_3.pdf) (accessed on 16 October 2019).
34. Geller, S.; Durand, J.L. Refinement of the structure of LiMnPO<sub>4</sub>. *Acta Cryst.* **1960**, *13*, 325–331. [CrossRef]
35. Herle, P.S.; Ellis, B.; Coombs, N.; Nazar, L.F. Nano-network electronic conduction in iron and nickel olivine phosphates. *Nat. Mater.* **2004**, *3*, 147–152. [CrossRef] [PubMed]
36. Sugiyama, J.; Nozaki, H.; Harada, M.; Kamazawa, K.; Ofer, O.; Månsson, M.; Brewer, J.H.; Ansaldo, E.J.; Chow, K.H.; Ikeda, Y.; et al. Magnetic and diffusive nature of LiFePO<sub>4</sub> investigated by muon spin rotation and relaxation. *Phys. Rev. B* **2011**, *84*, 054430. [CrossRef]
37. Menil, F. Systematic trends of the <sup>57</sup>Fe Mössbauer isomer shifts in (FeO<sub>n</sub>) and (FeF<sub>n</sub>) polyhedra. Evidence of a new correlation between the isomer shift and the inductive effect of the competing bond T-X (→ Fe) (where X is O or F and T any element with a formal positive charge). *J. Phys. Chem. Solids* **1985**, *46*, 763–789. [CrossRef]
38. Kündig, W. Evaluation of Mössbauer spectra for <sup>57</sup>Fe. *Nucl. Instrum. Methods* **1967**, *48*, 219–228. [CrossRef]
39. Cococcioni, M.; Marzari, N. Energetics and cathode voltages of LiMPO<sub>4</sub> olivines (M = Fe, Mn) from extended Hubbard functionals. *Phys. Rev. Mater.* **2019**, *3*, 033801. [CrossRef]

40. Sobolev, A.V.; Presniakov, I.A.; Gippius, A.A.; Chernyavskii, I.V.; Schaedler, M.; Buettgen, N.; Ibragimov, S.A.; Morozov, I.V.; Shevelkov, A.V. Helical magnetic structure and hyperfine interactions in FeP studied by  $^{57}\text{Fe}$  Mössbauer spectroscopy and  $^{31}\text{P}$  NMR. *J. Alloys Compd.* **2016**, *675*, 277–285. [[CrossRef](#)]
41. These angles obviously differ from the polar ( $\theta$ ) and azimuthal ( $\phi$ ) introduced in the context of MS spectral parameters.
42. Kara, M.; Kurki-Suonio, K. Symmetrized multipole analysis of orientational distributions. *Acta Cryst. A* **1981**, *37*, 201–210. [[CrossRef](#)]



© 2019 by the authors. Licensee MDPI, Basel, Switzerland. This article is an open access article distributed under the terms and conditions of the Creative Commons Attribution (CC BY) license (<http://creativecommons.org/licenses/by/4.0/>).